

On the Hot Embrittlement of Continuously-cast and Transfer-bar Structures in DP600 Advanced High-strength Steel

M.H. Ghoncheh¹, J. Sengupta², N. Wu², J. Gao², and A.B. Phillion¹

¹*Department of Materials Science and Engineering, McMaster University, Hamilton, ON L8S 4L7, Canada, ²ArcelorMittal Global R&D, Hamilton, ON L8N 3J5, Canada*

Keywords: Advanced high-strength steel (AHSS), Hot embrittlement, As-cast (AC), Transfer-bar (TB), Gleeble tensile testing

This article has been published in the Journal of Materials Processing Technology. The final publication is available at Elsevier via <https://doi.org/10.1016/j.jmatprotec.2020.116936>

Abstract

This study reports on ultra-high temperature tensile tests (1300 to 1480 °C) performed on dual-phase (DP) advanced high-strength steels utilizing a Gleeble 3500 thermo-mechanical simulator. The thermomechanical results of both as-cast (AC) and transfer-bar (TB) materials are presented, as well as three different sample geometries, to better comprehend the effect of temperature distribution and stress localization on the reproducibility of data. The results show that presence of pre-existing porosity in the AC structure decreases the ultra-high temperature strength of the material because of voids nucleation, growth and coalescence, while tearing apart of the melt in highly susceptible zones plays an important role to drastically increase the ultra-high temperature embrittlement of the TB material. It is shown that a sample with long-gauge-length (LGL) geometry provides the most consistent reproducibility as compared with other geometries; this is attributed to a combination between gentle stress localization and intensified temperature distribution along the gauge length.

I. Introduction

a. Dual-phase advanced high-strength steels

There is currently an increasing worldwide demand for advanced high-strength steels (AHSSs) in order to satisfy vehicle performance and safety while reducing green-house gas emissions. According to [Kuziak et al. \(2008\)](#), dual-phase (DP) steel, a successful AHSS grade with 0.06-0.15wt% C, 1.5-3wt% Mn, 0.05-0.2wt% Si as well as small amounts of microalloying elements (Nb, V, Cr, and Mo) is widely used in load-bearing parts of body-in-white i.e. the vehicle frame thanks to its high toughness and formability.

Prior to heat treatment to generate the DP microstructure, the alloy must be processed in the liquid state to achieve the desired alloy composition, and then continuously cast. As described by [Zhao and Jiang \(2017\)](#), the continuously-cast slab consists of as-cast microstructure, i.e. coarse columnar-dendritic morphology, macro- and micro- segregation, gas and shrinkage porosity. This slab is then reheated up to 1200 to 1320 °C and subsequently rough rolled. The product, called transfer bar material, shows better distribution of alloying elements into the matrix, and modified microstructure with reduced grain size and less porosity.

b. Hot embrittlement in continuously-cast products

According to [Thomas \(2002\)](#), the continuous casting process is often accompanied by process difficulties that bring extra costs to the fabrication cycle. In this category, hot embrittlement is one of the most well-known phenomenon. This defect was defined by [Mintz and Crowther \(2010\)](#) as a lack of ductility within 700-1200°C, when the steel product mostly contains austenite grains surrounded by a thin layer of ferrite along the γ grain boundaries. [Guo et al. \(2010\)](#) included cracking about the solidus temperature, where the liquid fraction is almost 1-10% and three phases (liquid, δ -ferrite and γ -austenite) are simultaneously present in the microstructure as another example of hot embrittlement. As illustrated in [Figure 1](#), the first type of embrittlement is mainly a

result of segregation of alloying elements to the γ grain boundaries. The second type of embrittlement, named as hot tearing by [Koshikawa et al. \(2016\)](#), is due to the low shear strength of liquid pockets that become isolated at the grain boundaries and triple junctions at the last stages of solidification. [Won et al. \(2000\)](#) described the brittle and ductile regions shown in [Figure 1](#) as:

- Zone (i): A zone of zero ductility at temperatures between the liquid impenetrable temperature (LIT) and the zero strength temperature (ZST), where the volume fraction of liquid is 70-75%. The response to deformation is transitioning from mass feeding to interdendritic feeding; the ZST is also called dendrite coherency point.
- Zone (ii): A zone of hot tearing susceptibility between the zero ductility temperature (ZDT) and the LIT in which the volume fraction of liquid is between 1 and 10%. The ZDT is also called mechanical coherency or rigidity point.
- Zone (iii): A zone of improved ductility below ZDT due to the formation of a monolithic solid structure as the last liquid solidifies.
- Zone (iv): A zone with good ductility at high temperature because of thermal softening phenomena like dynamic recovery (DRV), recrystallization (DRX), and grain boundary sliding (GBS) to reduce strain localization along the initial boundaries and prevent intergranular failure.
- Zone (v): A zone of severe embrittlement as a result of segregation of sulphur during solidification and precipitation of alloying elements, e.g. N and Al via solid-state diffusion along the γ grain boundaries.
- Zone (vi): A zone of good ductility due to the presence of an increase in the volume fraction of ferrite, $\geq 45\%$.

According to [Mintz and Crowther \(2010\)](#), past research has focused much effort on quantifying hot embrittlement at temperatures between 700-1200°C and above the solidus temperature (T_s). However, there has not been much study

of hot embrittlement in temperature range between 1200°C and T_s . As Rao et al. (1996) presented, softening mechanisms that were already active at lower temperatures become more competitive within this range, and the controlling mechanism for ductility and yield stress change based on thermal and geometrical factors. Moreover, Humphreys et al. (2017) reported that short-length diffusion paths through the γ grains will evolve to long-range diffusion due to the high diffusion rate, which spreads beyond neighbouring grains and causes GBS, while hardening becomes localized due to strain fields around high-temperature carbides or inclusions. In this study, a series of thermomechanical tests at temperatures between 1200-1480°C is performed to investigate the effects of microstructure on hot embrittlement in a DP600 AHSS alloy, as well as to quantify the yield strength and reduction-in-area for modelling purposes. The effect of three sample geometries, as well as material in the as-cast (AC) and transfer-bar (TB) conditions is explored.

II. Experimental Procedure

a. Material

The as-received material, taken from the surface of a continuously-cast slab in both the As-Cast (AC) and Transfer-Bar (TB) conditions and with the chemical composition given in Table 1, was provided by ArcelorMittal Dofasco (Hamilton ON). Samples were taken from the surface of the slab because of the fact that most continuous casting defects, e.g. oscillation marks and surface deflections, nucleate and propagate in that region. Since material in the AC state might have casting-related pores and very large grains, TB material experiencing a single pass rough rolling was also investigated to assess the effect of porosity and grain size on ultra-high temperature mechanical behaviour. An isopleth of the Fe-C phase diagram for an alloy with the specified composition is given in Figure 2 to identify the critical phase transformations of interest. As can be seen, the alloy goes through a peritectic reaction prior to complete solidification. The relevant transformation temperatures are given in Table 2; these

values were determined using a proprietary model developed by ArcelorMittal.

b. Ultra-High Temperature Tensile Testing

A Gleeble 3500 thermomechanical simulator was utilized to perform the hot tensile tests on the DP600 AHSS material. The sample geometry is discussed below. Temperature control during testing was achieved using a R-type thermocouple, placed at the centre each sample. In order to prevent severe oxidation of the hot-spot zone at high temperatures, a quartz tube was placed around the sample gauge region, while ultra-high purity argon gas (99.999%) was used to backfill the sample chamber. The reheating schedule is provided in Figure 3; samples were first reheated to 1400 °C and then held for a soaking time to provide consistent microstructure and temperature at the hot-spot zone; they were then cooled or heated to test temperature between 1300 and 1480 °C; and then deformed at a constant deformation rate of 0.002 cm.s⁻¹. For each condition (materials, sample geometry, and temperature), two tests were performed. A maximum test temperature of 1480 °C was chosen deliberately to be very close to the peritectic reaction, where γ and δ phases could be both stable and partial melting is inevitable. Due to propensity for thermocouple detachment during partial melting at 1480°C and subsequent termination of the test, the soaking time at 1400°C was decreased from 120 to 45 s for tests performed at this temperature. At the conclusion of the test the overall ductility was evaluated by quantifying the reduction in fracture area (RA),

$$RA(\%) = \frac{(A_0 - A_f)}{A_0} \times 100 \quad (1)$$

where A_0 and A_f represent the initial and fracture cross-sectional areas, respectively. The initial area was estimated using calipers while the final area was estimated from optical micrographs of the fracture surface.

c. Sample Geometry

A full series of tensile tests was performed on three different sample geometries, named No Gauge Length (NGL), Short Gauge Length (SGL), and

Long Gauge Length (LGL), with dimensions given in Figure 4. These samples were designed to investigate how temperature distribution and stress localization along the gauge affect the ultra-high temperature mechanical properties, i.e. the ductility and maximum tensile strength. The design of the NGL geometry relied upon homogenizing the longitudinal temperature distribution within a narrow central zone, and vice versa, for the LGL design. The SGL geometry, brought a sharp stress localization onto the sample’s shoulder due to the small radius of curvature as compared to the LGL design. For the SGL and LGL samples, a second thermocouple was added and placed adjacent to the onset of increase in sample diameter. Please note that the red marks in Figure 4 indicate the placement of the thermocouples.

d. Microstructural Evaluation

For optical metallography, the samples were mounted into a hot cured resin, ground and polished with a colloidal silica suspension using STRUERS Tegamin-25 machine, and chemically etched in 4% Nital (96 ethanol-4 nitric acid), and then analyzed using a KEYENCE vhx6000 microscopy. For fractography, the samples were cut cross-sectionally parallel to the fracture surface using a STRUERS Accotum-5 precision cutter, and then analyzed using a JEOL 6610lv scanning electron microscope. Energy-dispersive X-ray spectroscopy (EDS) was carried out to identify the locations and compositions of inclusions and low-melting phases distributed on the fracture surfaces.

III. Results and Discussion

a. Microstructural and thermal characteristics

Figure 5 (a and b) shows the microstructure of the as-cast (AC) material in the initial/untested state. As can be seen, it mainly consists of α -ferrite, pearlite with two morphologies, and retained austenite. The α -ferrite (shown in white) occupies a significant fraction of the microstructure. The decomposition of γ -austenite to pro-eutectoid α has lead to the formation of allotrimorphic

ferrite with polygonal morphology. The nucleation site for this type of ferrite is usually the primary γ grain boundaries because there is no other 2D heterogeneous nucleation site interior of the γ grains, and the growth direction is preferentially along the γ grain boundaries. Pearlite with monochromic black colour has formed from the γ as a result of eutectoid phase transformation. The zebra-pattern structure, known as degenerate pearlite, has formed under highly diffusion-controlled transformation conditions and contains thicker lamellas of ferrite within the vicinity of fine cementite particles. The occurrence of these two morphologies has been previously reported in continuously-cast C-Mn steels by [Thompson et al. \(2001\)](#), when cooling rates of $30\text{-}300^\circ\text{C}\cdot\text{s}^{-1}$ were applied. They reported that addition of Mn to steel leads to a drop in the activity of C in austenite, thereby promoting the formation of non-equilibrium degenerate pearlite. Finally, the retained austenite is distinguishable by its brown colour. [Timokhina et al. \(2004\)](#) showed that an increase in the Mn and Si content in some regions, caused by high temperature solute diffusion, has increased the probability of retaining γ due to reduction in carbon concentration. In this case, [Sugimoto et al. \(1992\)](#) investigated the effect of Mn and Si on volume fraction and stability of retained γ in TRIP-aided DP steels. They reported higher effectiveness of Mn than Si, where Mn lowers the T_0 temperature, while Si suppresses carbide precipitations.

Figure 5 (c and d) shows the initial microstructure of the transfer-bar (TB) material. As can be seen, the TB material includes neither fine lamellar pearlite nor retained austenite but instead consists mostly of small pockets of degenerate pearlite banded between α grains. As the rough rolling process at a temperature above $0.5T_m$ has resulted in dynamic recrystallization and elongation of the grains in the rolling direction, the result is α grains and pearlite pockets that are finer than those in the AC material. Also, the slow cooling rate during reheating and rough rolling in comparison to the $50^\circ\text{C}\cdot\text{s}^{-1}$ on the slab surface during continuous casting has provided sufficient time for long-range diffusion of C and thus a higher tendency to form degenerate pearlite rather than fine lamellar type.

As can be seen in Table 3, the average size of the ferrite grains is significantly decreased in the TB structure as compared to the AC state, while the pearlite fraction is increased due to the recrystallization and grain growth during reheating and rough rolling. These two subsequent phenomena facilitate the growth of numerous strain-free grains that have nucleated on the primary γ grain boundaries. Fine austenitic microstructure obtained by reheating has a higher tendency to form pearlite as compared with the coarse material that has rapidly cooled during continuous casting. Since the suitable substrate for the pearlite pockets to form is the γ grain boundaries, fine austenite grains result in a proliferation of pearlite.

b. Ultra-high temperature constitutive properties

Figure 6 shows the ultra-high temperature constitutive properties of the AC and TB materials; (a) shows examples of the measured stress/displacement curves at 1300 and 1400 °C for the AC material (two tests for each geometry at each temperature), while (b) and (c) provide the measured RA and maximum engineering stress (σ_{eng}^{max}) values for all temperatures. Beginning with (a), it can be seen that the measured engineering stress decreases with displacement beyond the stress peak, although a wavy/oscillatory response is observed. This is likely a result of discontinuous (cyclic) dynamic recrystallization (dDRX) in austenite because of the ultra-high temperatures and low strain rate. As defined by Lin et al. (2009), dDRX is a repetitive sequences of strain hardening and softening caused by nucleation of new recrystallized grains during deformation. According to Sakai et al. (2014), this phenomenon also shows a decrease in the flow stress with increasing displacement until a dynamic balance between strain hardening and strain softening is established. In the tests performed in this study the last part of dDRX (a balance between strain hardening and softening) is not achieved due to the low ductility. As can be seen in the figures, both the sample geometry and temperature significantly affect the measured RA and σ_{eng}^{max} . The reasons for this is discussed below. Please note that fewer tests were successfully performed at 1450 and 1480 °C than at 1300 and 1400 °C

because of difficulties with thermocouple detachment. Please also note that the RA% could not be reported at 1480 °C due to melting of the fracture surface, and consequently, an unrepresentative section area measurement.

Figure 7 provides a comparison between the temperatures recorded by at the centre and on the shoulder for the SGL and LGL samples. During testing, TC1 follows explicitly the applied thermal cycle, as it is the control thermocouple. TC2, however, shows a shallower heating rate as well as lower temperatures, with more of an effect in the LGL samples than in the SGL sample. Given the Joule heating of the Gleeble apparatus, and water cooling of the sample grips, a temperature distribution along the gauge at the start of deformation is inevitable. The temperature recorded by TC2 then decreases during the test due to displacement of the sample which decreases the cross-section of the gauge length thus decreasing the heat input required to maintain a constant temperature at TC1.

Thermomechanical behaviour of the LGL geometry

The results shown in Figure 6 demonstrate that the LGL sample geometry, in both the AC and TB states, provides a very good consistency between the results for each pair of tested samples at various temperatures. This consistency is due to a very gentle radius of curvature along its shoulder and consequently, almost homogeneous stress localization along the gauge length during testing. The temperature distribution between the centre position and shoulder, shown in Figure 7 is significant, which guarantees that the hot-spot zone during testing will take place on the middle of the gauge. Both characteristics govern a situation in which samples tend to show the sharp localized necking rather than diffuse necking, defined by [Melander and Husby \(1980\)](#) as the stress during tensile testing decreases slowly with displacement due to the occurrence of a balance between strain hardening and thermal softening mechanisms in several regions. [Tang et al. \(2016\)](#) also used a sample geometry similar to the LGL geometry and presented consistent constitutive data in a 0.22wt.%C-1.25wt.%Mn-0.005wt.%B steel alloy. Although the results of their damage evolution model

were in a good accordance with experimental data, medium-to-high test temperatures (550-850 °C) that they used are increased to ultra-high temperatures in this research to check data reproducibility. The localized heating on the central part of this geometry with a small gauge diameter makes the samples vulnerable to melting even at temperatures that are significantly lower than $T_{solidus}$; this is due to an adjustment between the heat input during the Gleeble testing and the temperature recorded on the sample's surface, so the core of sample experiences higher temperature. The same mechanism was also reported by [Sheykh-jaberi et al. \(2019\)](#), where they compared the semi-solid ($0.95 < f_s < 1.0$) constitutive behaviour of A356 and B206 aluminum alloys. In [Figure 6](#), an increase in the test temperature results in a decrease in σ_{eng}^{max} , as expected. [Lin et al. \(2009\)](#) showed in 42CrMo steels, the increased temperature intensifies the rate of dislocations annihilation, the number of vacancies and their diffusion rate, grain growth, and dissolution of high-temperature precipitates and carbides in the γ phase, which all can lead to a drop in peak stress.

Except for those samples tested at 1400 °C, σ_{eng}^{max} is higher in the TB samples as compared with the AC samples. The RA data, on the other hand, is quite scattered at all temperatures. As the TB samples show high susceptibility to localized melting (see [Figure 8](#)), the variability in RA is further increased. In terms of higher melting tendency of the TB samples, it is hypothesized that the larger area fraction of the grain boundaries even after the growth of the recrystallized grains in these samples as compared with the coarse grains of the AC samples increases the Gibbs free energy. Therefore, the TB-LGL sample will be exposed to severe melting at 1450 °C, while the AC-LGL at the same temperature is subjected to only partial melting mostly happening at the triple junctions or the last zones to have solidified during continuous casting.

At lower temperatures, the stress relief in triple junctions as a result of severe dynamic recovery (DRV) in the AC samples postpones stress localization during the test, but the dependency of void growth and coalescence on temperature neutralizes the effect of DRV at 1400 °C, so the RA at 1300 °C is almost the same as 1400 °C. σ_{eng}^{max} , on the other hand, shows improvement at both 1400 and

1480 °C compared with 1450 °C. Its increase at 1400 °C is a result of intensified void deformation before failure, while the scenario at 1480 °C is related to the γ to δ reverse transformation that is accompanied by an increase in lattice volume, shrinkage in voids, thermally-grooved boundaries, and generation of dislocations due to transformation stresses. [Dippenaar and Phelan \(2003\)](#) also presented the occurrence of some microstructural changes e.g. thermal grooving, sub-boundaries evolution, and peritectic transformation in 3Cr12 steel by means of high-temperature laser-scanning confocal microscopy. Although the rate of DRV in δ is much higher than γ , reported by [McQueen and Jonas \(1975\)](#), the explanation mentioned above leads to an increase in the stress peak at 1480 °C. The reasons presented for the trends of failure and maximum stresses in the AC samples can be valid for the TB samples, as well. On the effect of temperature on the RA, the minimum values at 1300 and 1450 °C can be assigned to the augmented dynamic recrystallization (DRX) coupled with partial melting, and severe localized melting, respectively.

Thermomechanical behaviour of the NGL geometry

As shown in Figure 6(a), the AC-NGL samples tested at 1300 °C revealed a steep loss in load at the end of deformation. [Rusinek and Rodriguez-Martinez \(2009\)](#) showed that the void-coalesced mode of fracture is identified by a drastic drop in σ value within a narrow range of displacement at the near-final stage of tensile testing. Therefore, this steep drop in the flow stress can be attributed to the dominance of void formation, growth and coalescence leading an inhomogeneous softening.. The TB-NGL samples show more susceptibility to diffuse necking since the whole part of the middle zone, with a very gentle decrease in diameter, is exposed to nearly the same temperature. In TB samples, there is no preferential weak zone in which the sharp necking can be initialized. Notwithstanding the same sample geometry, the AC samples are prone to sharp localized necking due to preexisted porosities. Both the AC and TB samples are seen to show a very similar trend in σ_{eng}^{max} , which does not vary significantly between 1300 and 1450 °C. In the matter of the RA, both structures present

the maximum value at 1400 °C resulting from high DRV rate and subsequently subgrain-, and grain growth at the expense of diminishing the maximum stress. Decreasing the RA and σ_{eng}^{max} values at 1450 °C are a result of tearing apart the material containing (melted) liquid films around the solid grains.

Thermomechanical behaviour of the SGL geometry

Comparing the results of the tests performed on the SGL samples with two previous geometries reveals that the numbers of data points, and data reproducibility, is low. This is because many of the Gleeble tests failed due to sample fracture in the shoulder and/or early failure prior to reaching the testing temperature. The underlying reason is the sample geometry, as the steep slope of increasing diameter within the gauge length shoulder results not only in higher localized stress, but also significantly affects the rate of void growth and coalescence due to stress triaxiality. In this regard, the effect of stress triaxiality on the void volume fraction has been discussed in detail by [Lassance et al. \(2006\)](#). They developed a mathematical model to simulate the growth and coalescence of penny-shaped voids at various levels of stress triaxiality during axisymmetric loading conditions. As the temperature increases, the RA and stress peak data σ_{eng}^{max} follow a diverging trend because of this stress triaxiality. Thus, a discussion on this geometry relating the results to the underlying thermomechanical mechanisms cannot be provided.

c. Fracture Analysis

Effect of sample geometry

Figure 8 shows fractographs, at two magnifications, of TB samples tested at 1300 °C. As can be seen, the TB-NGL sample shows lower susceptibility to melting, just on the tips of paraboloid-shape zones (marker (i)), while the decrease in gauge diameter to the TB-LGL sample increases partial melting intensity due to higher temperature localization. The reason behind the rosette-shape dendrite in the TB-LGL sample is the melting of interdendritic regions solidified at lower temperatures during the continuous casting process. Solute rejected ahead of the

solid/liquid interface during the solidification leads to the formation of highly concentrated solid surrounding the primary dendrite arms. The fracture mode in the TB-NGL sample is ductile somewhere associated with void nucleation and growth. The LGL sample shows brittle mode due to tearing apart of the melt that is formed in high volume fraction. The TB-SGL sample presents an intermediate condition, combination of ductile and brittle modes (marker (iii)), however, the presence of some grain de-cohesion (marker (ii)) is ascribed to the stress localizing due to its sharp-shoulder geometry. Finally, as shown in the TB-LGL fractograph, although the interdendritic cavity can be filled up by the melt due to high penetrability of the liquid, the melt cannot withstand against the tensile load. The localization of temperature through the melt increases the probability of exposing to higher temperature in the core of the sample. Consequently, the pliable material loses its viscosity associated with melting of low-concentrated solid material (marker (iv)). To put this simply, [Bakhtiyarov and Overfelt \(1999\)](#) showed that the liquid formed very close to the peritectic tie-line is very pasty, however, an increase in temperature provides more liquid fraction with less viscosity. In terms of the RA mean value, the TB-NGL, TB-SGL, and TB-LGL transfer-bar samples show almost 25, 27, and 14% at 1300 °C (see Figure 6). Note that although this discussion has focused on the TB material, similar observations were made from the fractographs of the AC material; only the TB material results were reported for brevity.

Effect of Test Temperature

Figure 9 shows fractographs, at two magnifications, of the AC-NGL samples tested at 1300 °C and 1400 °C. The first observable difference is coarsening of the structure at 1400 °C due to the grain growth phenomenon. While the dominant mechanism at 1300 °C is severe DRX, the sample tested at 1400 °C shows higher intensity of the DRV and grain growth. The less melting susceptibility of the AC material compared with the TB samples can be confirmed in this figure by focusing on the highly magnified triple junction at 1400 °C (bottom-right subfigure). As seen, the edge of each grain keeps its sharp morphology

with no irregular deformation, which identifies a lack of melting at the triple junctions. The governing deformation mechanism at 1400 °C is thus clearly grain sliding due to weakening of the boundaries at high DRV rate, while for the sample at 1300 °C, void growth and coalescence are dominant (upper-left subfigure). Another reason behind the grain sliding at 1400 °C can be concluded from the results reported by [Vetrano et al. \(1999\)](#), where they in-situ heated samples under the transmission electron microscope to observe disequilibrium of vacancies at high temperatures due to formation and coalescence of nanocavities at the vicinity of the grain boundaries. According to [Reed \(2008\)](#), to avoid vacancy clustering, the grains move over each other to consume a portion of generating vacancies and contribute superplasticity, same as a mechanism during power-law creep. Both structures show ductile fracture accompanied by high RA. In this case, the AC-NGL shows almost 33% mean RA, and 20 MPa stress peak at 1300°C, while 27% mean RA and 13 MPa stress peak are achieved at 1400°C (see [Figure 6](#)).

d. Effective parameters on hot embrittlement

The effective parameters that determine the mode of fracture in the AC and TB materials (i.e. the critical microstructural features) are the partial melting of the matrix, as well as the presence of both low-melting temperature phases and high-temperature inclusions. As previously discussed, based upon the test temperature, sample geometry, the as-received microstructure, the tensile specimen will experience temperature localizing through its necking zone, which brings partial or at higher severity, localized melting. The presence of liquid leads to early onset failure that intensifies the tendency to hot embrittlement. In terms of the ductility, the low volume fraction of the melt associated with higher viscosity is suitable by filling the voids formed and coalesced during constitutive deformation, while [Li et al. \(2016\)](#) mentioned that higher volumes with increase in fluidity can be easily pulled apart during testing and cause brittle fracture. [Figure 10](#) demonstrates this effect; having a higher solute content the interdendritic regions are more prone to melting due to a lower melting temperature as

compared with the primary branches of dendrites. As indicated by an arrow, a pasty-like plastic deformation before the rupture is concurrently occurred at the vicinity of the regions torn apart due to interdendritic melting. This means that there has been a small portion of the matrix in the TB-LGL sample that can barely impede against the tensile loading even at the lowest test temperature in this study (1300°C).

Figure 11 shows an EDS analysis of the TB-LGL sample, identifying the presence of S-rich precipitates embedded in the fracture surface. According to Weinberg (1997), these phases form at a temperature much lower than the steel's solidus, thus they will remelt during Gleeble testing. By spreading along and wetting the austenite grain boundaries, the S-rich precipitates weaken the shear strength of the material thus causing embrittlement at ultra-high temperatures. In this regard, Mostefa et al. (1991) showed that sulfur segregation at high temperatures is usually taken place adjacent to the tip of microcracks, promotes their propagation, and subsequently, intergranular brittleness. In other words, a combination between tensile stress and high temperature enhances the contribution of the intergranular sliding to the total deformation, however, the sulfur intergranular segregation deteriorates the hot ductility. Finally, as can be seen in Figure 12, there has been a round-shape inclusion shown with BSE and SE analyses, and precipitated in the triple junction. The high intensity of calcium in the EDS result confirms that this inclusion should not be as a reaction product between the alloying elements preexisted in the composition. As Wang et al. (2002) expressed, during steel processing in the ladle, the Ca element is intentionally added to the melt to prevent nozzle clogging during the continuous casting. The product is formed as an $[\text{Al}_2\text{O}_3\text{-CaO}]/\text{CaS}$ core/shell inclusion preventing nozzle clogging, and ameliorating the fracture and fatigue strength by reducing the sulfur content, if it can be removed by floating through the slag. Otherwise, its non-metallic surface is not able to be wet by the melt during solidification and consequently the disbonded interface causes air gap formation during shrinkage by solidification and phase transformation, which was also observed by Campbell (2017). He named these entrapped oxide films

as bifilms, which can be enlarged due to the trapped gas expansion at high temperature and constitute microcracks required to initiate failure. This gap was also identified by [Brimacombe et al. \(1997\)](#) as a nucleation site for crack formation and propagation. Since these precipitates are stable even at ultra-high temperatures, they act as a barrier against dislocations mobility, causing dislocation piles up and stored stress, as [Sommitsch et al. \(2002\)](#) reported.

As a brief summary, the LGL geometry showed the best reproducibility of data for each microstructure tested at 1300, 1400, 1450, and 1480°C. Also, the LGL samples were successfully tested over the proposed temperature interval and showed meaningful results, which can be further used as a representative sample showing the AHSSs embrittlement manner through all three brittle zones in the continuous casting process. Apart from that, the TB LGL samples revealed better mechanical properties compared with the AC samples, resulting from the absence of microprositities in their structure.

IV. Conclusions

The Gleeble thermomechanical simulator is used to measure constitutive properties of DP600 at ultra-high temperatures and determine a suitable sample geometry that proposes better hot ductility and strength. The most important contributions of this research are concluded as,

- The coarse-grain AC structure mainly contains ferrite, retained austenite, and pearlite formed in two styles of fine and coarse degenerate, while the TB material shows fine ferrite and degenerate pearlite pockets.
- The LGL samples show better reproducibility of the data due to the smooth stress localization along their gauge and the steep temperature distribution that exposes the middle of the gauge to the highest temperature, called hot-spot zone. The synergy between two mentioned factors conducts a condition in which the LGL samples neck sharply on their middle section followed by an uneven plastic deformation and ultimately failure.

- The SGL samples show the lowest convergence between the data due to a high stress triaxiality localized beneath the sharp shoulder. The NGL geometry, on the other hand, presents a very gentle stress localization due to the absence of the gauge, but the hot-spot zone cannot take place in a specific zone, and consequently the necking diffuses from one zone to another. The diffuse necking mode brings lower repeatability in the data compared with the LGL geometry.
- On the effective parameters on ultra-high temperature mechanical behaviour, the presence of non-metallic inclusions and low melting phases facilitate hot embrittlement based upon void formation and tearing apart of wet γ grain boundaries at temperatures lower than solidus temperature.

V. Acknowledgment

Research funding provided by ArcelorMittal and the Natural Sciences and Engineering Research Council of Canada. Discussions with Bruce Farrand and Brian Nelson at ArcelorMittal are also gratefully acknowledged.

VI. Tables

Table 1: Chemical composition of the DP600 AHSS alloy examined in this study, wt%

C	Mn	Si	Cr	Mo	Ti	S	P	Al
0.1	1.54	0.18	0.19	0.22	0.02	0.002	0.01	0.05

Table 2: Critical transformation temperatures of the DP600 AHSS alloy examined in this study

	Liquidus	Peritectic	Solidus
ArcelorMittal	1519°C	1483°C	1476°C

Table 3: Ferrite grain size and pearlite fraction in the AC and TB materials

Material	α grain size (μm^2)	Pearlite frac- tion (%)
As-cast	5727	19
Transfer-bar	679	30

VII. Figure Headings

Figure 1: Schematic diagram of the hot embrittlement zones in plain C-Mn and C-Mn-(low)Al steels

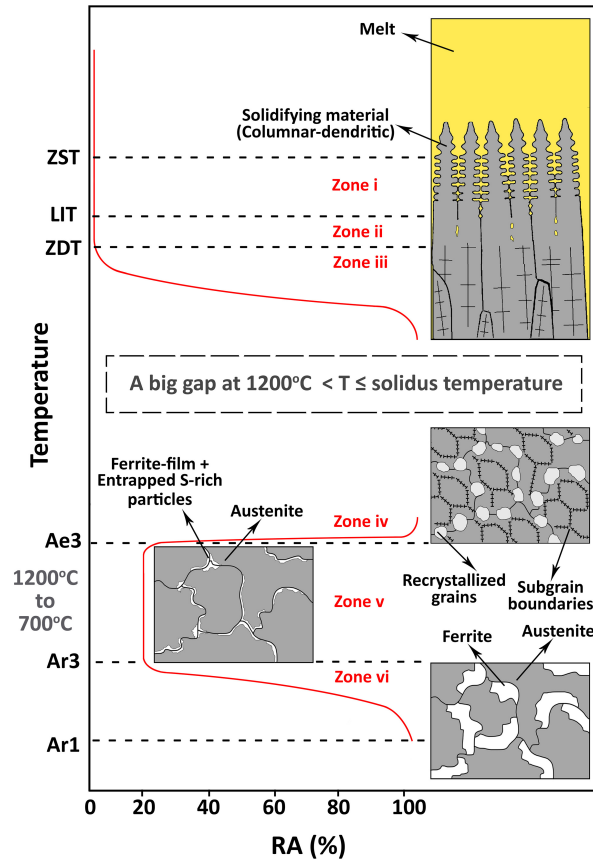


Figure 2: Fe-C isopleth at constant Cr, Mn, Mo, Ti, and S, over the temperature interval investigated in this study

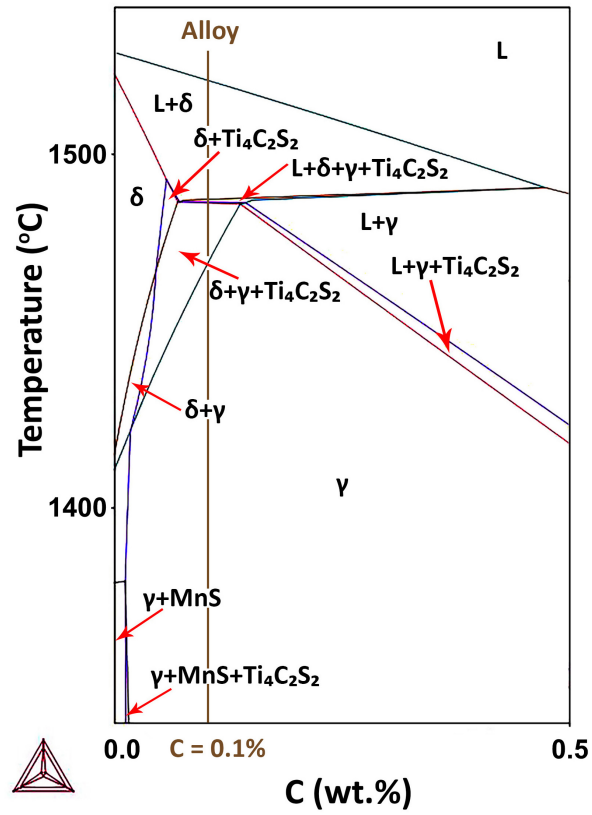


Figure 3: Thermomechanical schedule applied to the DP600 AHSS samples

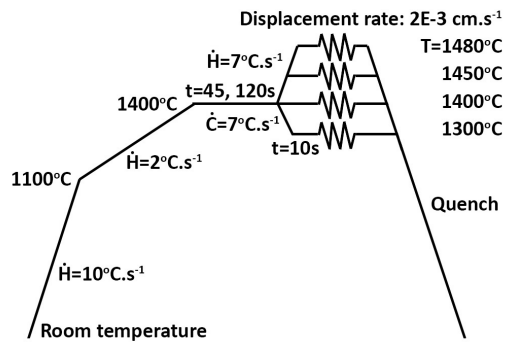


Figure 4: Schematic of the three tested sample geometries. The red circles indicates the placement of the thermocouples. Dimensions given in mm

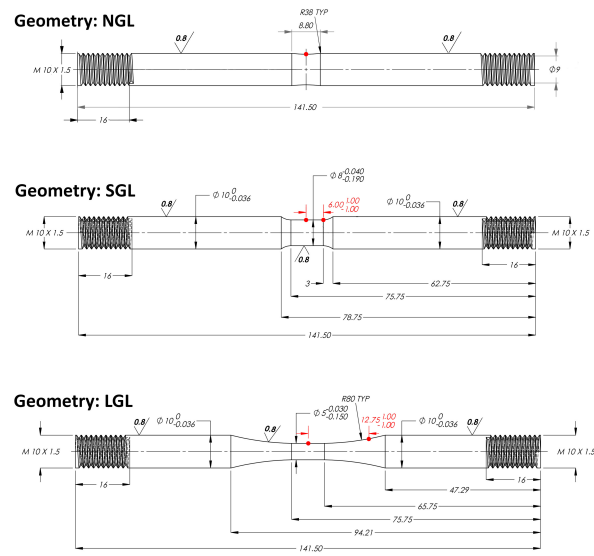


Figure 5: Optical micrographs of the (a and b) AC, and (c and d) TB materials at two magnifications

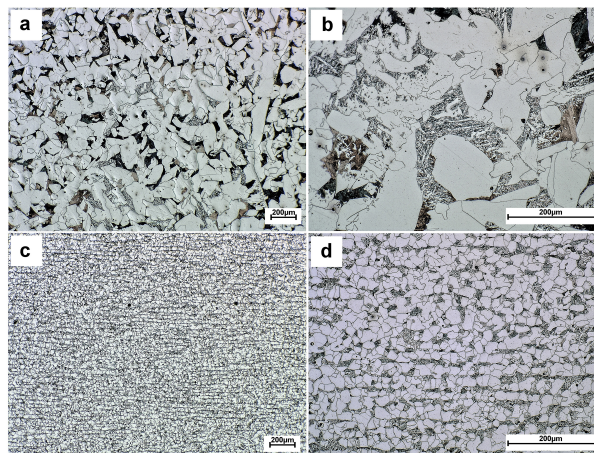


Figure 6: (a) the constitutive data achieved for the as-cast samples, and the corresponding (b) reduction of area, and (c) peak stress values (dashed and straight lines at 1300 and 1400 °C, hollow and filled symbols for the TB and AC materials, respectively)

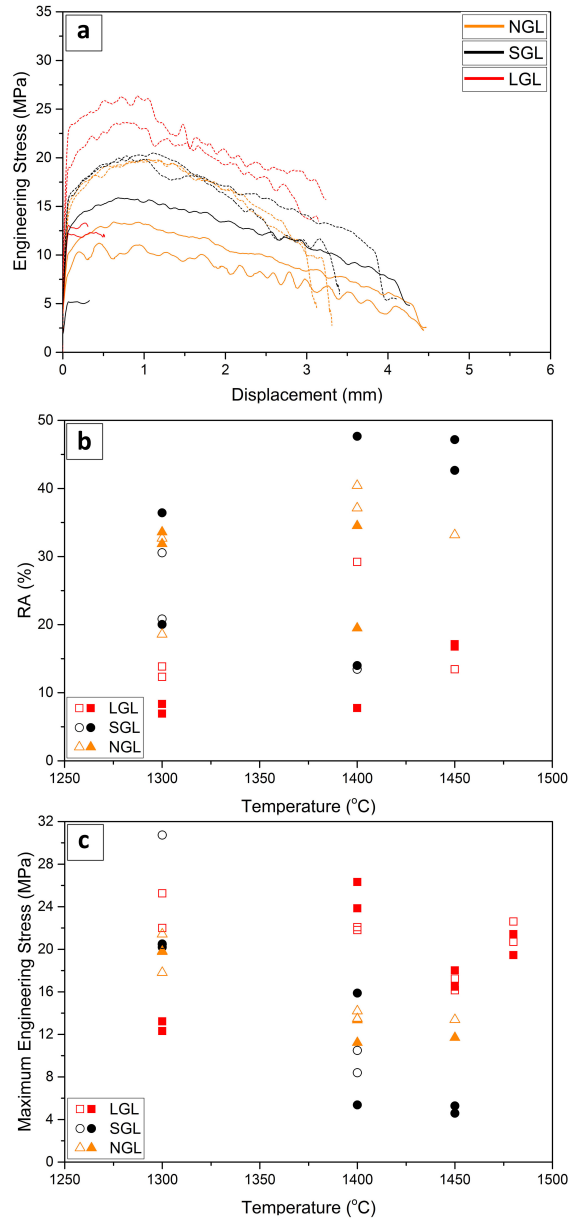


Figure 7: Temperature measurements at 1300°C test temperature (straight lines: TB-SGL, and dashed lines: TB-LGL samples)

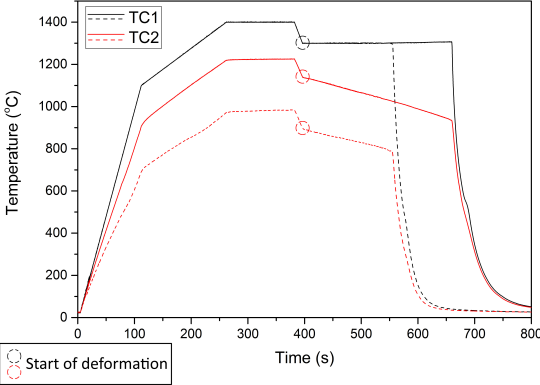


Figure 8: Fractographs of transfer-bar samples tested at 1300 °C (Rows from top to bottom: NGL, SGL, LGL geometries at two magnifications - (i) paraboloid-shape zone, (ii) structure decohesion, (iii) brittle fracture, (iv) interdendritic melting)

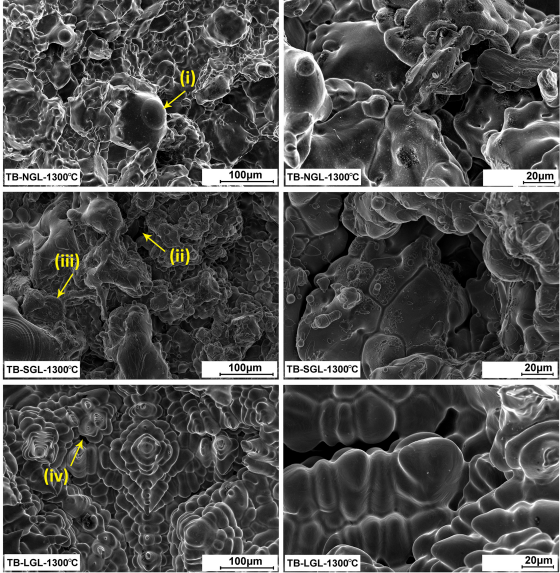


Figure 9: Fractographs of as-cast NGL samples at two magnifications (Left column: tested at 1300°C, and Right column: tested at 1400°C)

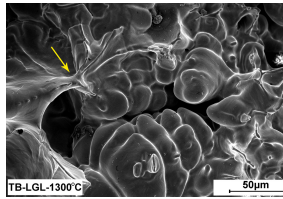
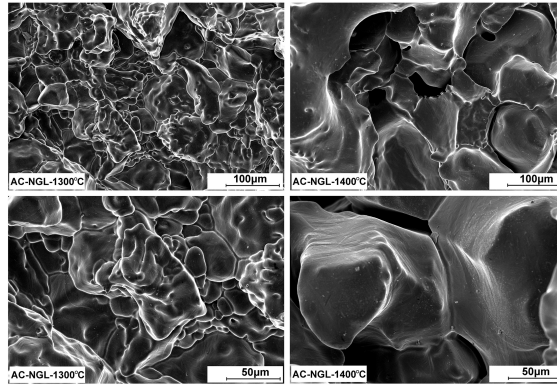
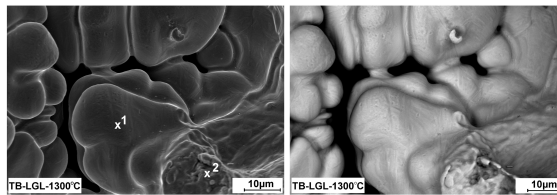


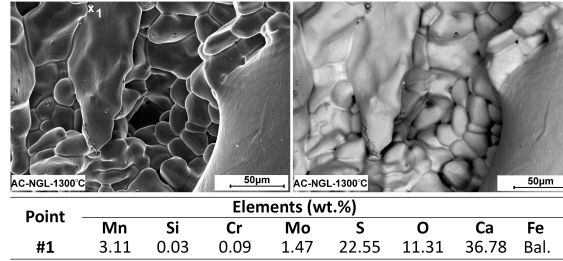
Figure 10: Partial melted zones in the TB-LGL sample tested at 1300°C

Figure 11: Sulfur-rich phase in the TB-LGL sample tested at 1300°C, and corresponding EDS results of the primary and low-melting phases.



Point	Elements (wt.%)						Fe
	Mn	Si	Cr	Mo	S	O	
#1	2.02	0.25	0.29	0.31	0.13	0.78	Bal.
#2	1.40	0.58	0.64	0.73	1.13	22.84	Bal.

Figure 12: Entrapped inclusion in the TB-LGL sample tested at 1300°C, and corresponding EDS results.



VIII. References

- Bakhtiyarov, S., Overfelt, R., 1999. Measurement of liquid metal viscosity by rotational technique. *Acta materialia* 47 (17), 4311–4319.
- Brimacombe, J., Weinberg, F., Hawbolt, E., 1979. Formation of longitudinal, midface cracks in continuously-cast slabs. *Metallurgical Transactions B* 10 (2), 279–292.
- Campbell, J., 2017. Melting, remelting, and casting for clean steel. *steel research international* 88 (1), 1600093.
- Dippenaar, R. J., Phelan, D. J., 2003. Delta-ferrite recovery structures in low-carbon steels. *Metall. Mater. Trans. B.* 34 (5), 495–501.
- Guo, L., Li, W., Bobadilla, M., Yao, M., Shen, H., 2010. High temperature mechanical properties of micro-alloyed carbon steel in the mushy zone. *steel research international* 81 (5), 387–393.
- Humphreys, J., Rohrer, G. S., Rollett, A., 2017. *Recrystallization and related annealing phenomena*. Elsevier.
- Koshikawa, T., Bellet, M., Gandin, C.-A., Yamamura, H., Bobadilla, M., 2016. Study of hot tearing during steel solidification through ingot punching test and its numerical simulation. *Metall. Mater. Trans. A.* 47 (8), 4053–4067.
- Kuziak, R., Kawalla, R., Waengler, S., 2008. Advanced high strength steels for automotive industry. *Arch. Civ. Mech. Eng.* 8 (2), 103–117.
- Lassance, D., Scheyvaerts, F., Pardoën, T., 2006. Growth and coalescence of penny-shaped voids in metallic alloys. *Eng. Fract. Mech.* 73 (8), 1009–1034.
- Li, G., Yu, W., Cai, Q., 2016. Investigation of reduction pretreatment process for continuous casting. *J. Mater. Process. Technol.* 227, 41–48.

- Lin, Y., Chen, M., Zhong, J., 2009. Study of metadynamic recrystallization behaviors in a low alloy steel. *Journal of Materials Processing Technology* 209, 2477–2482.
- McQueen, H., Jonas, J., 1975. Recovery and recrystallization during high temperature deformation. In: *Treatise. Mater. Sci. Technol.* Vol. 6. Elsevier, pp. 393–493.
- Melander, A., Husby, K.-O., 1980. Influence of the strain rate sensitivity of diffuse necking in tensile tests. *Mater. Sci. Eng.* 46 (1), 103–112.
- Mintz, B., Crowther, D. N., 2010. Hot ductility of steels and its relationship to the problem of transverse cracking in continuous casting. *Int. Mater. Rev.* 55 (3), 168–196.
- Mostefa, L. B., Saindrenan, G., Solignac, M., Colin, J., 1991. Effect of interfacial sulfur segregation on the hot ductility drop of FeNi36 alloys. *Acta metallurgica et materialia* 39 (12), 3111–3118.
- Rao, K., Prasad, Y., Hawbolt, E., 1996. Hot deformation studies on a low-carbon steel: Part 1 - flow curves and the constitutive relationship. *Journal of Materials Processing Technology* 56, 897–907.
- Reed, R. C., 2008. *The superalloys: Fundamentals and applications.* Cambridge University Press.
- Rusinek, A., Rodriguez-Martinez, J., 2009. Thermo-viscoplastic constitutive relation for aluminium alloys, modeling of negative strain rate sensitivity and viscous drag effects. *Mater. Design.* 30 (10), 4377–4390.
- Sakai, T., Belyakov, A., Kaibyshev, R., Miura, H., Jonas, J. J., 2014. Dynamic and post-dynamic recrystallization under hot, cold and severe plastic deformation conditions. *Prog. Mater. Sci.* 60, 130–207.
- Sheykh-jaberi, F., Cockcroft, S., Maijer, D., Phillion, A., 2019. Comparison of the semi-solid constitutive behaviour of a356 and b206 aluminum foundry alloys. *Journal of Materials Processing Technology* 266, 37–45.

- Sommitsch, C., Wieser, V., Kleber, S., 2002. A dislocation density model for the simulation of hot forming processes. *Journal of Materials Processing Technology* 125-126, 130–137.
- Sugimoto, K.-i., Usui, N., Kobayashi, M., Hashimoto, S.-i., 1992. Effects of volume fraction and stability of retained austenite on ductility of TRIP-aided dual-phase steels. *ISIJ. Int.* 32 (12), 1311–1318.
- Tang, B., Bruschi, S., Ghiotti, A., Bariani, P., 2016. An improved damage evolution model to predict fracture of steel sheet at elevated temperature. *J. Mater. Process. Technol.* 228, 76–87.
- Thomas, B. G., 2002. Modeling of the continuous casting of steel—Past, present, and future. *Metall. Mater. Trans. B.* 33 (6), 795–812.
- Thompson, M., Ferry, M., PA, M., 2001. Simulation of hot-band microstructure of C–Mn steels during high speed cooling. *ISIJ. Int.* 41 (8), 891–899.
- Timokhina, I., Hodgson, P., Pereloma, E., 2004. Effect of microstructure on the stability of retained austenite in transformation-induced-plasticity steels. *Metall. Mater. Trans. A.* 35 (8), 2331–2341.
- Vetrano, J., Simonen, E., Bruemmer, S., 1999. Evidence for excess vacancies at sliding grain boundaries during superplastic deformation. *Acta materialia* 47 (15-16), 4125–4129.
- Wang, Y., Sridhar, S., Valdez, M., 2002. Formation of CaS on Al₂O₃-CaO inclusions during solidification of steels. *Metall. Mater. Trans. B.* 33 (4), 625–632.
- Weinberg, F., 1979. The ductility of continuously-cast steel near the melting point—hot tearing. *Metallurgical Transactions B* 10 (2), 219–227.
- Won, Y. M., Yeo, T.-J., Seol, D. J., Oh, K. H., 2000. A new criterion for internal crack formation in continuously cast steels. *Metall. Mater. Trans. B.* 31 (4), 779–794.

Zhao, J., Jiang, Z., 2017. Rolling of advanced high strength steels: Theory, simulation and practice. CRC Press.